

PAPER • OPEN ACCESS

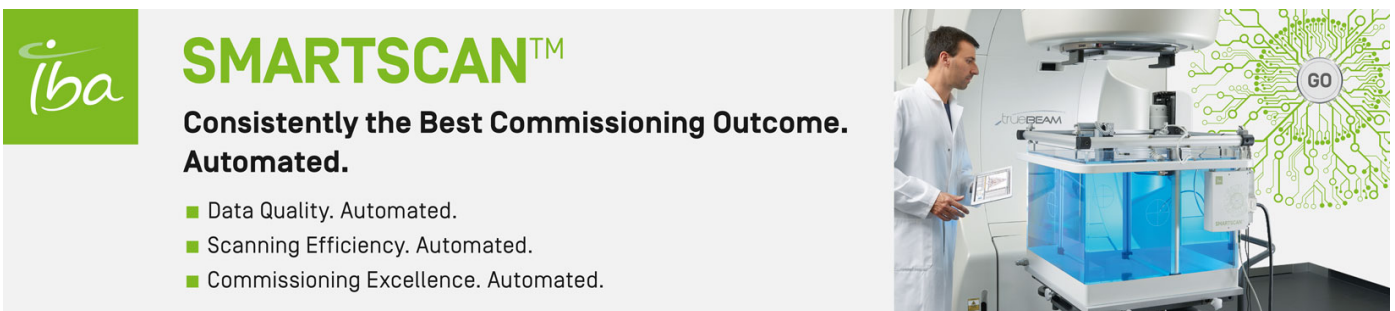
Performance of a dual-layer scanner for hybrid SPECT/CBCT

To cite this article: Martijn M A Dietze *et al* 2019 *Phys. Med. Biol.* **64** 105020

View the [article online](#) for updates and enhancements.

Recent citations

- [Accelerated SPECT image reconstruction with FBP and an image enhancement convolutional neural network](#)
Martijn M. A. Dietze *et al*
- [A comparative study of NaI\(Tl\), CeBr₃ and CZT for use in a real-time simultaneous nuclear and fluoroscopic dual-layer detector](#)
Wilco J C Koppert *et al*



 **SMARTSCAN™**

Consistently the Best Commissioning Outcome. Automated.

- Data Quality. Automated.
- Scanning Efficiency. Automated.
- Commissioning Excellence. Automated.



OPEN ACCESS

PAPER



Performance of a dual-layer scanner for hybrid SPECT/CBCT

RECEIVED
7 January 2019REVISED
1 April 2019ACCEPTED FOR PUBLICATION
4 April 2019PUBLISHED
16 May 2019Martijn M A Dietze^{1,2,3}, Britt Kunnen^{1,2}, Sandra van der Velden^{1,2}, J H Leo Steenbergen¹, Wilco J C Koppert¹, Max A Viergever² and Hugo W A M de Jong^{1,2}¹ Radiology and Nuclear Medicine, Utrecht University and University Medical Center Utrecht, PO Box 85500, 3508 GA, Utrecht, The Netherlands² Image Sciences Institute, Utrecht University and University Medical Center Utrecht, PO Box 85500, 3508 GA, Utrecht, The Netherlands³ Author to whom any correspondence should be addressed.E-mail: m.m.a.dietze@umcutrecht.nl

Keywords: SPECT, CBCT, dual-layer, radioembolization

Original content from this work may be used under the terms of the [Creative Commons Attribution 3.0 licence](https://creativecommons.org/licenses/by/3.0/).

Any further distribution of this work must maintain attribution to the author(s) and the title of the work, journal citation and DOI.



Abstract

Fluoroscopic procedures involving radionuclides would benefit from interventional nuclear imaging by obtaining real-time feedback on the activity distribution. We have previously proposed a dual-layer detector that offers such procedural guidance by simultaneous fluoroscopic and nuclear planar imaging. Acquisition of single photon computed tomography (SPECT) and cone beam computed tomography (CBCT) could provide additional information on the activity distribution. This study investigates the feasibility and the image quality of simultaneous SPECT/CBCT, by means of phantom experiments and simulations.

Simulations were performed to study the obtained reconstruction quality for (i) clinical SPECT/CT, (ii) a dual-layer scanner configured with optimized hardware, and (iii) our (non-optimized) dual-layer prototype. Experiments on an image quality phantom and an anthropomorphic phantom (including extrahepatic depositions with volumes and activities close to the median values encountered in hepatic radioembolization) were performed with a clinical SPECT/CT scanner and with our dual-layer prototype. Nuclear images were visually and quantitatively evaluated by measuring the tumor/non-tumor (T/N) ratio and contrast-to-noise ratio (CNR).

The simulations showed that the maximum obtained CNR was 38.8 ± 0.8 for the clinical scanner, 30.2 ± 0.9 for the optimized dual-layer scanner, and 20.8 ± 0.4 for the prototype scanner. T/N ratio showed a similar decline. The phantom experiments showed that performing simultaneous SPECT/CBCT is feasible. The CNR obtained from the SPECT reconstruction of largest sphere in the image quality phantom was 43.1 for the clinical scanner and 28.6 for the developed prototype scanner. The anthropomorphic phantom showed that the extrahepatic depositions were detected with both scanners.

A dual-layer detector is able to simultaneously acquire SPECT and CBCT. Both CNR and T/N ratio are worse than that of a clinical system, but the phantom experiments showed that extrahepatic depositions with volumes and activities close to the median values encountered in hepatic radioembolization could be distinguished.

Introduction

In recent years, significant progress has been made in the development of hybrid medical scanners. For instance, single photon emission computed tomography (SPECT) scans are now routinely corrected for photon attenuation by using the included computed tomography (CT) component of SPECT/CT devices (Ritt *et al* 2014). Together with software improvements in e.g. scatter correction and resolution modeling, SPECT/CT is increasingly considered a quantitative modality (Bailey and Willowson 2014). These improvements have initiated new opportunities in the evaluation of administered activity (Bailey and Willowson 2013).

For example, in hepatic radioembolization, where yttrium-90 (⁹⁰Y) labeled microspheres are injected into the liver (Kennedy *et al* 2012, Braat *et al* 2015), a separate pre-treatment fluoroscopy-guided interventional

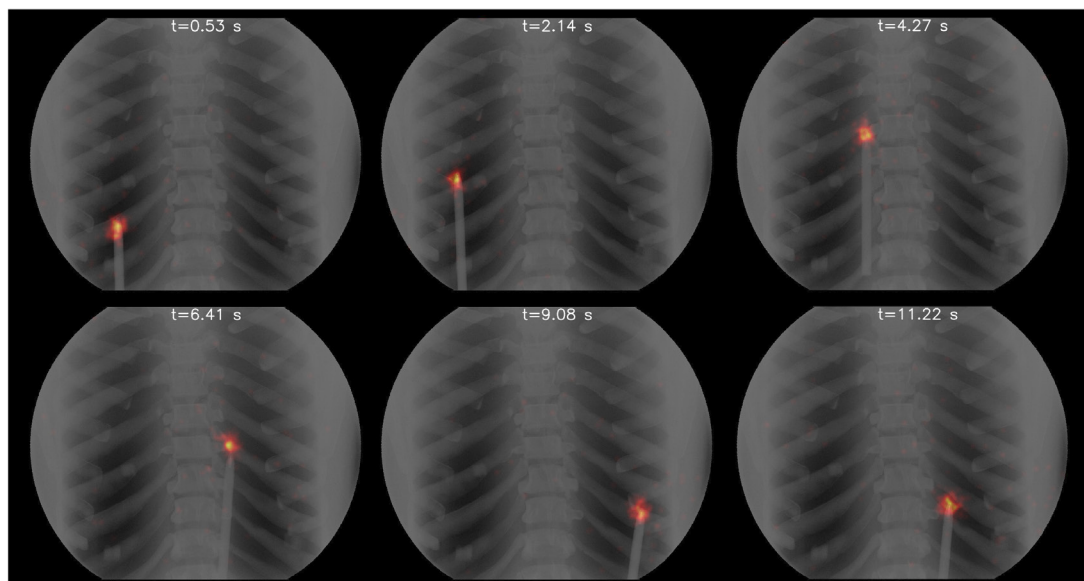


Figure 1. An illustration of how nuclear (color) and fluoroscopic (gray-scale) information is captured simultaneously in planar imaging. A cobalt-57 pen marker was moved inside the thorax of an anthropomorphic phantom. Details of the acquisition can be found elsewhere (van der Velden *et al* 2019).

procedure with technetium-99m-labeled macroaggregated albumin (^{99m}Tc -MAA) is performed. After this procedure, the lung shunt fraction and potential extrahepatic depositions are determined on SPECT/CT to decide whether the treatment can safely continue. Ideally, the results from this SPECT/CT scan would be directly available during the interventional procedure, so that both ^{99m}Tc pre-treatment and ^{90}Y treatment administrations could be merged into a single fluoroscopic interventional session (Gabr *et al* 2016).

However, the activity distribution can currently only be visualized using the scanners at the nuclear medicine department. Evaluation during the fluoroscopic interventional session would thus require patients to be transferred across the hospital, which takes a substantial amount of time. Additionally, the catheter used to inject activity could shift in position, creating an unintended difference in the vascular flow (and thus in the distribution) between several administrations (Garin *et al* 2016). The combination of these effects makes transportation unattractive for clinical practice; a dedicated scanner in the intervention room would be preferred.

With this application in mind, a compact hybrid scanner (van der Velden *et al* 2019) was previously proposed. The dual-layer detector, consisting of a cone beam CT (CBCT) flat panel positioned in front of a gamma camera, can acquire nuclear and fluoroscopic projections with the same field of view (FOV) simultaneously (see figure 1 for an example). The use of a C-arm gantry resulted in a compact scanner that would enable seamless integration in the intervention room. For hepatic radioembolization, this means that both anatomy and activity distribution could be simultaneously visualized. Such information is currently not available and could aid radionuclide administration by offering direct feedback to the physician.

The proposed dual-layer scanner has been evaluated for a 2D setting (i.e. planar imaging). Additional information on the activity distribution can be achieved if a complete rotation around the patient is performed; resulting in a hybrid SPECT/CBCT. Quantitative results can then be retrieved by including attenuation and scatter correction in the SPECT reconstruction. The dual-layer scanner has potential advantages over a clinical SPECT/CT system by achieving intrinsically registered reconstructions (as the detectors capture the same FOV at the same time) and compensation for respiratory motion in the SPECT reconstruction (exploiting the simultaneous nature of the acquired projections).

Since there exist substantial differences in system design between the dual-layer scanner and a clinical SPECT/CT scanner, the SPECT reconstruction quality of the dual-layer scanner will be lower. The extent of this is, however, currently not clear. For our proposed specific application in hepatic radioembolization, image quality requirements could be relaxed as compared with a diagnostic SPECT/CT scan. Accordingly, the lower quality of the dual-layer scanner would not necessarily impede clinical usage in interventional procedures.

This study evaluates the image quality and quantitative accuracy of the dual-layer scanner in comparison to a clinical SPECT/CT scanner via simulations and phantom experiments. For the simulations, the dual-layer design will be evaluated for our developed (non-optimized) prototype and for a scanner optimized for gamma transmission, to illustrate the potential future capabilities of the dual-layer design.

Table 1. Configurations of the clinical scanner, the optimized dual-layer scanner, and the prototype dual-layer scanner, evaluated in this study.

	Clinical	Optimized	Prototype
Mobile	No	Yes	No
Detector heads	Two	One	One
CT acquisition	Separate	Simultaneous	Simultaneous
Detector orbit	Body-tracing	Parameterized	Circular
Flat panel transmission	—	65%	52%
Flat panel thickness	—	2.0 cm	7.5 cm
Collimator	Parallel hole (LEHR)	Cone beam (LEHR)	Cone beam (Custom)
Gamma camera FOV	$53.3 \times 38.7 \text{ cm}^2$	$60.0 \times 45.0 \text{ cm}^2$	$40.0 \times 24.0 \text{ cm}^2$

Methods

Studied scanners

This study compared the performance of three scanners, whose configurations are shown in table 1.

Clinical SPECT/CT

The clinical SPECT/CT scanner was a Symbia T16 (Siemens Healthineers, Erlangen, Germany). This scanner has two detector heads, was mounted with a low-energy high-resolution (LEHR) parallel hole collimator (24.05 mm hole length, 1.11 mm hole diameter and 0.16 mm septal thickness) and is able to perform a body-tracing orbit. The effective FOV of the gamma camera was $53.3 \times 38.7 \text{ cm}^2$. The CT scan is always performed separately from the SPECT scan. Intrinsic spatial resolution was 3.8 mm full width at half maximum (FWHM) and the energy resolution was 9.9% (Siemens 2010).

Optimized dual-layer

The proposed dual-layer scanner is shown in figure 2. A flat panel detector is positioned in front of a gamma camera with cone beam LEHR collimator with 100 cm focal distance. The x-ray tube is positioned at 100 cm from the collimator, so that nuclear and fluoroscopic projections capture the same FOV. The majority of x-rays are absorbed in the flat panel, whilst the gamma photons are, due to their relatively higher energy, more likely to pass through the flat panel and be detected by the gamma camera. This hybrid scanner can, due to its compact configuration, be mounted on a custom C-arm.

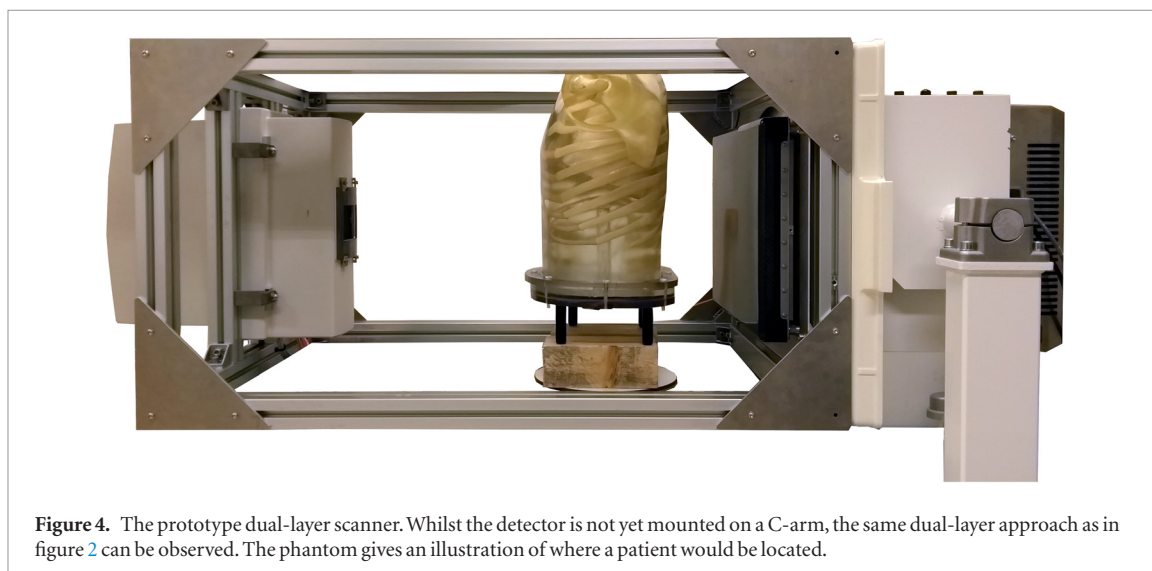
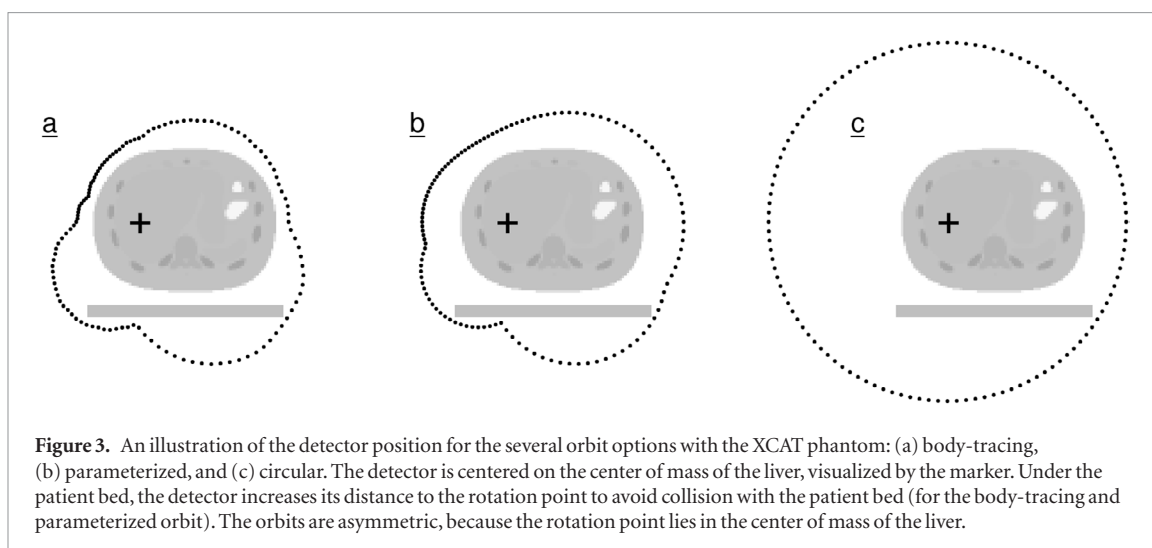
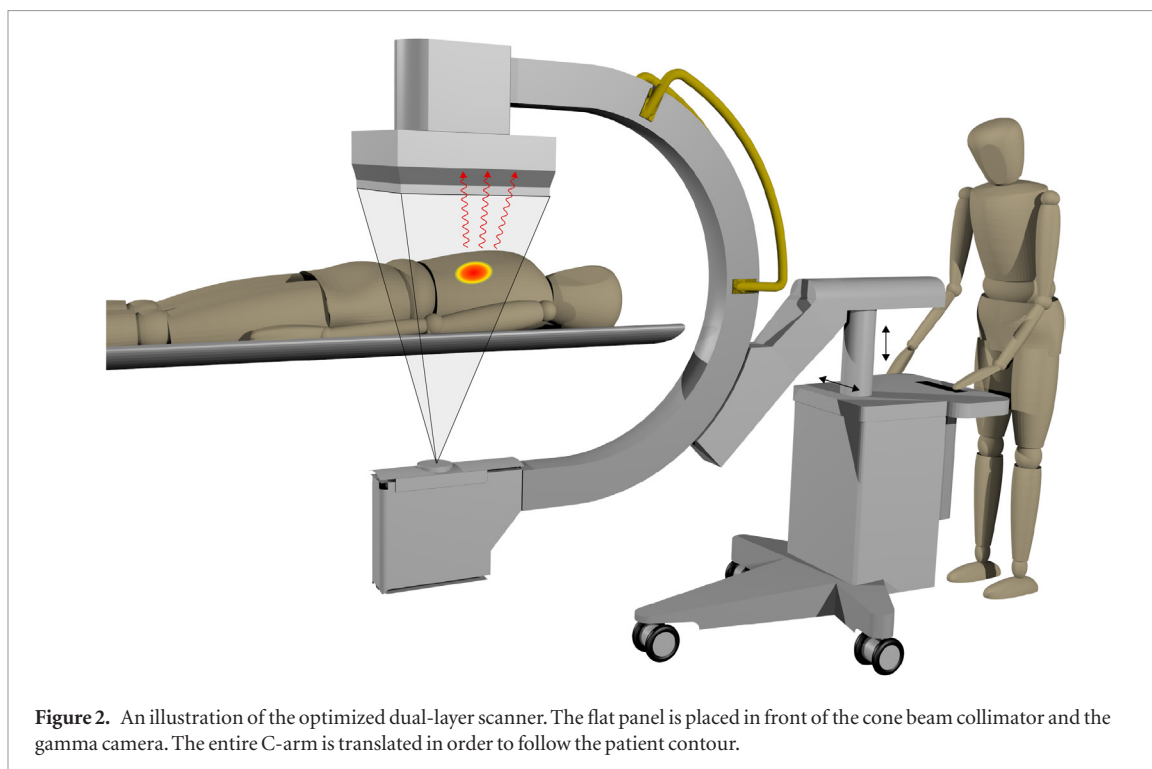
Only one detector head will be present on the dual-layer scanner, which increases the noise levels in comparison with the clinical SPECT/CT scanner with two detector heads. The introduction of the flat panel in front of the gamma camera also decreases the number of detected gamma photons. The expected gamma transmission for an optimized flat panel (2 cm in thickness) at 140 keV is between 65 and 73% (van der Velden *et al* 2019); transmission of 65% was chosen for this study. The effective FOV of the gamma camera would need to be somewhat larger than a clinical scanner, to account for the cone geometry; a FOV of $60.0 \times 45.0 \text{ cm}^2$ is likely sufficient. The gamma camera was assumed to have the performance as in the prototype dual-layer scanner: intrinsic spatial resolution of 3.1 mm FWHM and energy resolution of 9.3%.

No collision monitors will be present on the scanner, in order to keep the design simple. This means that a regular body-tracing orbit will not be performed. Rather, by measuring the detector-patient distance at a few points, a parameterized orbit can be constructed (see figure 3 for an illustration). Such an orbit is not optimal, since it needs to account for many possible patient shapes and sizes, but will be substantially better in tracking the patient contour than a circular orbit.

Prototype dual-layer

The developed prototype scanner, see figure 4, was configured with the same dual-layer approach as in figure 2, but was not yet mounted on a C-arm. The phantom was therefore positioned on a rotating table, which means that a circular orbit was performed. The gamma camera and the flat panel were positioned as close to each other as possible. The focal spot of the x-ray tube (Veradius; Philips Healthcare, Best, The Netherlands) was positioned at 98 cm from the front of the cone beam collimator and was aligned with the center of the detectors.

The used flat panel was adjusted from a commercially available product (Pixium 3040; Trixell, Moirans, France) by reducing the thickness of the back shielding plate, which resulted in a gamma transmission rate of 52% at 140 keV (van der Velden *et al* 2019). The flat panel thickness was 7.5 cm and the effective FOV was $38.2 \times 29.6 \text{ cm}^2$. The difference with an optimized flat panel (as above) comes from the printed circuit board electronics that would ideally be placed outside of the detector by extending the flat cables, which would allow for a more compact detector housing.



No adjustments were made to the gamma camera (P3000; Inter Medical Medizinservice, Lübbecke, Germany), which had an effective FOV of $40.0 \times 24.0 \text{ cm}^2$, intrinsic spatial resolution of 3.1 mm FWHM, and energy resolution of 9.3%. The cone beam collimator was custom-made and had a focal distance of 98 cm, 40.00 mm hole length, 1.90 mm hole diameter and 0.25 mm septal thickness. These hole dimensions were slightly larger than those of a regular LEHR collimator (but had approximately the same aspect ratio), owing to limitations of the manufacturing process.

Simulation study

There are substantial differences in hardware between the clinical SPECT/CT scanner and the dual-layer scanners. The effects of the differences on the final nuclear reconstruction quality were evaluated in a simulation study. The simulation study functions as a reference for observed performance in the phantom experiments, finds the influence of individual components, evaluates the expected performance of the optimized design, and allows a more rigorous evaluation than with the phantom experiments.

The XCAT phantom (Segars *et al* 2010) was used for the creation of realistic digital patient data, using the standard settings of a 95 kg male. The phantom contained a total of 150 MBq $^{99\text{m}}\text{Tc}$, in which a tumor with respectively 20, 30 or 50 mm radius was added at an uptake ratio of 5.0:1.0. Activity in the lungs was added at a lung-shunting fraction (LSF) of 5.00%. A flat patient bed (as in the intervention room) was positioned 5 cm underneath the phantom. The activity and attenuation maps were configured on a $240 \times 240 \times 300$ matrix, with 4.7 mm isotropic voxels. Attenuation maps were assumed to be known perfectly from the CT or CBCT scan, hence no effects from these maps on SPECT reconstruction were included.

The Utrecht Monte Carlo System (UMCS) (de Jong *et al* 2001, Dietze *et al* 2018b) was used to generate projections. UMCS simulates the photon physics and detector response in a fast manner, making it possible to acquire noise-free projections. The required collimator point spread functions were generated in GATE (Jan *et al* 2004) for every detector configuration. The effects of measurement time and nuclear activity were incorporated by addition of Poisson noise to the projections. The gamma camera was centered on the liver center-of-mass.

Simulated scan time was 10 min, as is what we envision for interventional procedures. Projections were simulated with 120 angles and photons were captured in an energy window of 15% around the 140 keV photopeak. Reconstructions were performed with ten iterations and eight subsets and a post-reconstruction Gaussian filter of 2.5 mm FWHM was applied. The effects of potential truncation in SPECT reconstructions owing to the different gamma camera sizes were not taken into account, as it was previously shown that truncation does not influence the accuracy of imaging in the region seen by all angles (Dietze *et al* 2018b). Ten noise realizations were performed per setting to study the stability of the various measures.

Reconstruction quality was compared on tumor to non-tumor (T/N) ratio (a crucial measure for dosimetry) and contrast-to-noise ratio (CNR) (as a measure of the visual quality). The T/N ratio was measured at iteration 10. The reported CNR was the maximum retrieved value over all iterations, inasmuch as CNR is a trade-off between recovered activity and background noise and will differ as a function of reconstruction convergence rate. Tumor and background liver masks were available from the initial phantom creation. The background liver mask was eroded by two voxels to reduce partial volume effects.

The clinical scanner was taken as the initial configuration for the simulations. The impact of changing an individual scanner component was hence evaluated for the decrease of detector heads from two to one, for the change of detector orbits from body tracing to parameterized or circular, for the introduction of a flat panel in front of the gamma camera, and for changing the collimator from parallel to cone beam. Furthermore, the three scanners, with all individual components combined together (e.g. for the prototype dual-layer scanner: one head, circular orbit, prototype flat panel, and prototype cone beam collimator), were also simulated.

Phantom study

A phantom study was performed to illustrate the image quality retrieved by the prototype dual-layer scanner and to evaluate the impact of simultaneous imaging. A custom image quality phantom and a realistic anthropomorphic phantom were scanned on both the clinical scanner and the developed prototype scanner. Images of the used phantoms are shown in figure 5.

The image quality phantom consisted of the spheres from a regular image quality (IQ) phantom (37, 28, 22, 17, 13, and 10 mm diameter) (IEC NEMA 2007) in their usual pattern, but they were enclosed in a different cylinder (Hoffman Brain phantom). The latter was used because it is somewhat smaller than the regular IQ enclosing, which ensured that no truncation effects affected the acquisition. The spheres were filled with an uptake ratio of 10.0:1.0 compared with the background compartment. The spheres and background were filled with water and a total of 150 MBq $^{99\text{m}}\text{Tc}$ was used.

The anthropomorphic phantom was modified from a commercially available phantom (Anthropomorphic Torso Phantom: ECT/TOR/P) by inclusion of a sphere with cold core (18.6 ml active volume, 5.6:1.0 uptake ratio relative to the background liver insert of 1200 ml) inside the liver and three spheres (4.1, 7.9, and 15.7 ml, all with



Figure 5. The used phantoms in this study. On the left, the image quality phantom, which was used to study the resolution and noise of the scanners. On the right, the anthropomorphic phantom, which is clinically relevant.

2.8:1.0 uptake ratio) in the torso. The lungs were filled with 5.4% of the total activity. The phantom was filled with water and a total of 160 MBq ^{99m}Tc was present. The phantom was configured in this way to represent the median volume (6.8 ml) and activity (1.3% of the total injected activity) of extrahepatic depositions encountered in hepatic radioembolization (Prince *et al* 2015).

In the prototype scanner, the rotation was continuous and the CBCT scan was performed simultaneously with SPECT at an acquisition rate of 3.75 Hz, hence 2250 x-ray projections were taken. The list mode SPECT data was binned into 120 projections. The image quality phantom was scanned using 50 kVp, 4 mAs, and 13.5 cm rotation radius. The anthropomorphic phantom was scanned using 60 kVp, 12 mAs, and 20.5 cm rotation radius. Reconstructions of the fluoroscopic projections were performed with the GPU-based iterative CBCT reconstruction TIGRE toolbox (Biguri *et al* 2016), using the SIRT algorithm with 50 iterations. The resulting CBCT reconstruction was used as attenuation map by applying a previously made look-up table.

For the clinical scanner, the SPECT (in step-and-shoot mode) and CT data were acquired sequentially. Again, 120 SPECT projections were acquired. The clinical scanner used 110 kVp with 14 mAs or 68 mAs for the image quality and anthropomorphic phantom, respectively. The attenuation maps were retrieved by means of the clinical software. Nuclear scanning time was 10 min for both scanners.

Since the anthropomorphic phantom did not fit completely into the prototype FOV, it could only be partially reconstructed. The resulting CBCT reconstruction was hence registered to the attenuation map of the clinical scanner by performing a rigid transformation with Elastix (Klein *et al* 2010). The clinical attenuation map could in this way be used for SPECT reconstruction of the prototype. Such a registration would also be required in a clinical interventional setting if the same size flat panel is used.

Nuclear reconstructions for both the prototype and the clinical scanner were performed using UMCS. A photopeak window of 15% around 140 keV was used and ten iterations with eight subsets were performed. For the prototype scanner, the pulses of the x-ray tube were cut from the SPECT list mode data by applying temporal selection to ensure only gamma photons were used. The anthropomorphic phantom was reconstructed on $128 \times 128 \times 128$ grid (voxel size of 4.79 mm), because this setting is currently used in clinical practice in our institute. The IQ phantom was reconstructed on a $256 \times 256 \times 256$ grid (isotropic voxel size of 2.40 mm), because this smaller voxel size allowed a more detailed visualization. A post-reconstruction Gaussian filter of 2.5 mm FWHM was applied to both SPECT reconstructions.

For the image quality phantom, T/N ratio and CNR were calculated. Lesion masks were made by thresholding the SPECT reconstruction to determine the spheres' centers of masses and then growing the volumes to the reported sphere sizes. The background volume was created by thresholding the active volume, removing the sphere masks and eroding the resulting mask by three voxels. For the anthropomorphic phantom, the reconstructions were solely visually assessed.

Results

Simulation study

Examples of reconstructions from the simulation study are shown for illustration purposes in figure 6 for the clinical, optimized, and prototype scanners. The clinical and optimized scanners generated the sharpest reconstructions, whereas the reconstruction was blurrier for the prototype scanner.

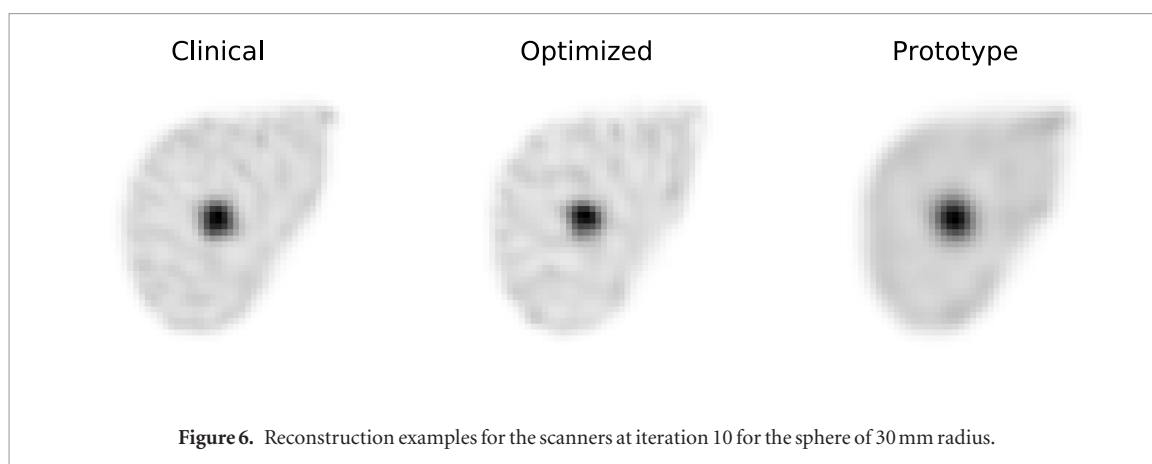


Figure 6. Reconstruction examples for the scanners at iteration 10 for the sphere of 30 mm radius.

Table 2. Overview of the results from the simulation study by changing a specific component with regards to the clinical scanner and by combining all individual components. Reported are the T/N ratios at iteration 10 for several tumor sizes, maximum CNR for the sphere of 30 mm radius, and LSF also for the phantom with 30 mm sphere. Uptake ratio in the phantom was 5.0:1.0 and LSF was 5.00%.

	T/N ratio			Max CNR	LSF [%]
	20 mm	30 mm	50 mm		
Clinical scanner	3.88 ± 0.16	4.28 ± 0.05	4.64 ± 0.03	37.6 ± 1.5	5.10 ± 0.03
Single detector head	3.95 ± 0.13	4.27 ± 0.08	4.66 ± 0.03	30.1 ± 0.9	5.04 ± 0.05
Parameterized orbit	3.80 ± 0.12	4.24 ± 0.06	4.64 ± 0.04	36.6 ± 1.2	5.12 ± 0.03
Circular orbit	2.81 ± 0.12	3.95 ± 0.07	4.40 ± 0.03	28.8 ± 0.7	5.25 ± 0.03
Optimized flat panel	3.71 ± 0.17	4.20 ± 0.05	4.60 ± 0.03	33.2 ± 1.3	5.10 ± 0.02
Prototype flat panel	3.53 ± 0.19	4.06 ± 0.05	4.51 ± 0.03	28.4 ± 1.1	5.11 ± 0.07
LEHR cone beam collimator	3.87 ± 0.11	4.27 ± 0.04	4.64 ± 0.04	42.2 ± 1.2	5.16 ± 0.03
Custom cone beam collimator	3.81 ± 0.12	4.28 ± 0.05	4.64 ± 0.02	43.2 ± 1.3	5.18 ± 0.03
Optimized scanner	3.74 ± 0.11	4.19 ± 0.06	4.59 ± 0.04	31.2 ± 1.2	5.16 ± 0.04
Prototype scanner	2.38 ± 0.07	3.68 ± 0.10	4.24 ± 0.03	22.0 ± 1.0	5.39 ± 0.05

The effect on reconstruction quality of the individual scanner components and the components combined into the scanner configurations are collected in table 2. The maximum CNR and LSF are reported solely for the 30 mm tumor, since these measures were less dependent on sphere size than T/N ratio.

The change in going from two detector heads to one resulted in higher noise levels in the reconstruction, since the time per view was halved. Therefore, CNR decreased for the dual-layer scanners. This reduction could be corrected for if the total scan time would be doubled. T/N ratio was largely unaffected by the number of detector heads.

Body tracing allowed the detector to get closest to the patient body, the parameterized orbit needed somewhat more space to account for all possible patients, and the circular orbit had a radius of 34 cm. When the gamma camera was positioned further away from the patient, the system resolution decreased. The T/N ratio and the CNR, therefore, both became worse in the dual-layer designs.

The effects on the reconstruction of introducing a flat panel were twofold. First, although the resolution recovery was incorporated in the reconstruction, the system resolution still decreased, because the thickness of the flat panel induced a larger phantom distance. Second, the number of detected nuclear counts reduced as a consequence of the attenuation of gamma photons. Therefore, both the T/N ratio and the CNR decreased when introducing a flat panel in front of the gamma camera.

The introduction of cone beam collimators improved noise levels somewhat compared with the parallel hole collimator, thanks to the increased system sensitivity. The CNR was thus increased. However, this improvement in reconstruction quality was negligible as compared with the effects of the other studied detector components. T/N ratio was largely unaffected, inasmuch as the system resolution remained the same.

Finally, all individual changes were combined to assess their joint influence on the image quality of the several studied scanners. Evidently, the clinical scanner had the best performance. The prototype possessed lower T/N ratios and lower CNR. The optimized dual-layer scanner had a lower CNR, but T/N ratios approached that of the clinical scanner.

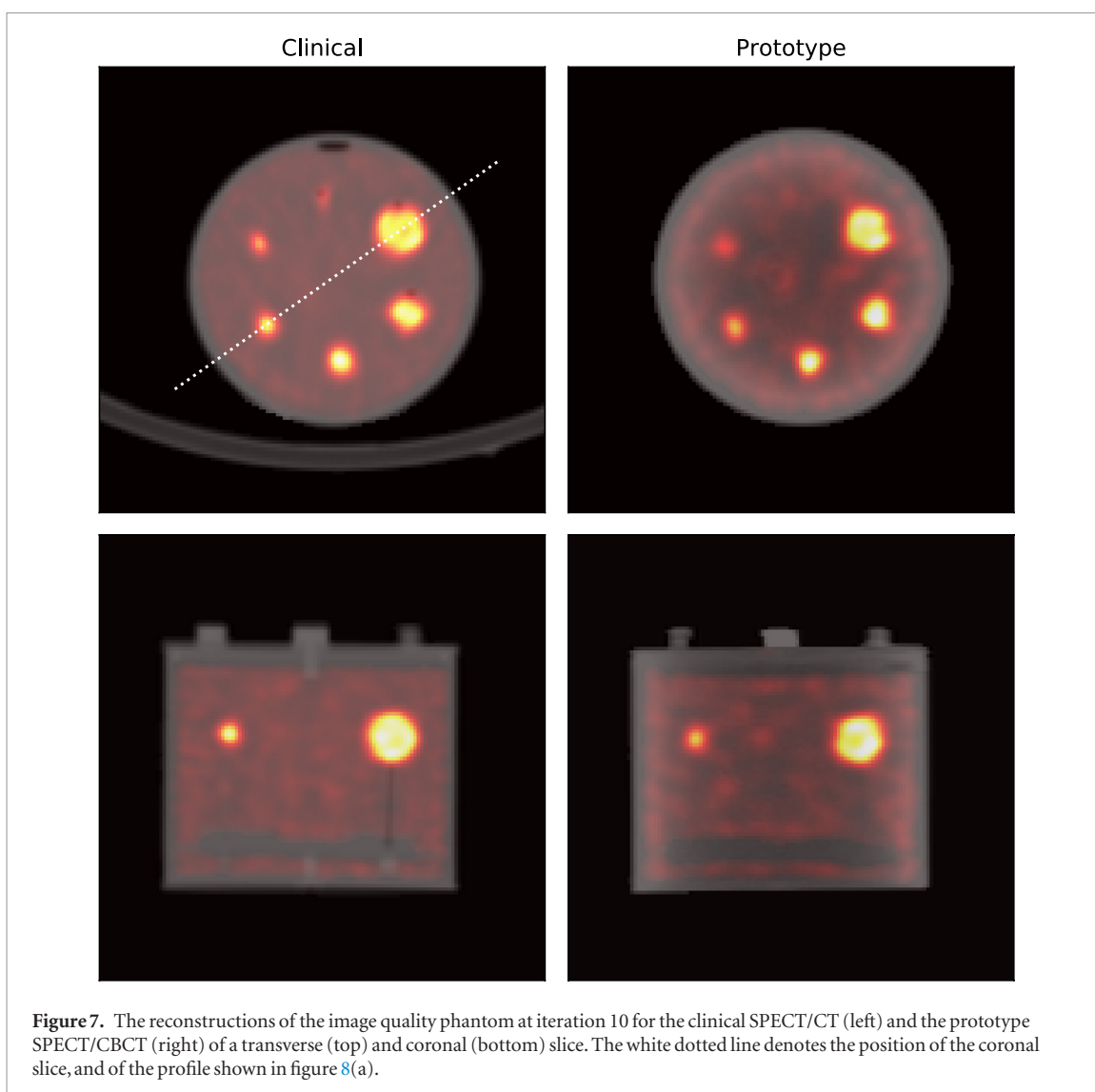


Figure 7. The reconstructions of the image quality phantom at iteration 10 for the clinical SPECT/CT (left) and the prototype SPECT/CBCT (right) of a transverse (top) and coronal (bottom) slice. The white dotted line denotes the position of the coronal slice, and of the profile shown in figure 8(a).

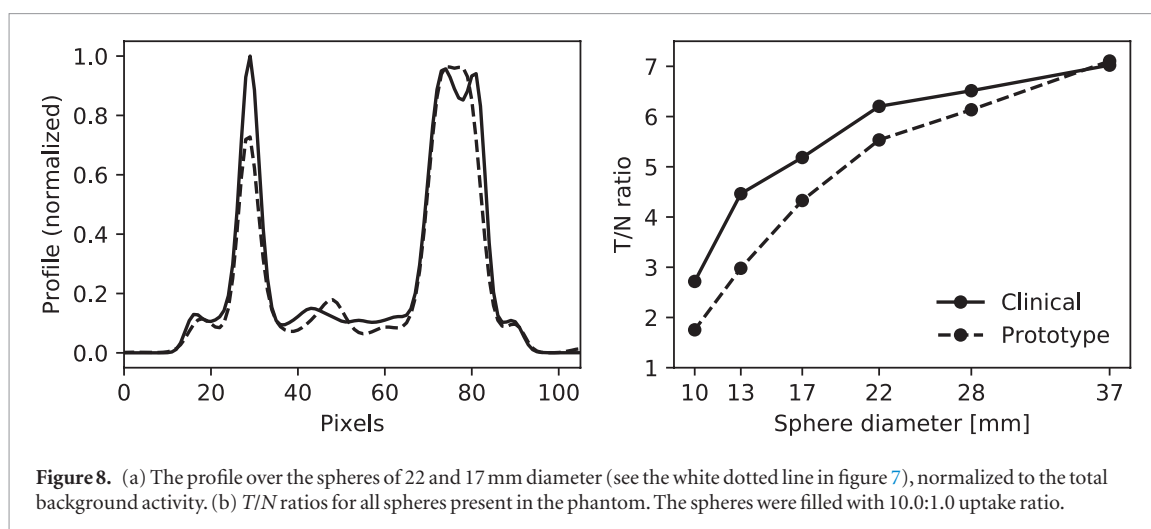
Phantom study

The reconstructions of the image quality phantom for the clinical and prototype scanners are shown in figure 7. The CBCT reconstructions made with the prototype scanner had no patient bed present, but the phantom showed the same shape and values as in the clinical scanner and was thus used for attenuation correction. The maximum CNR of the largest sphere in the reconstruction was 43.1 for the clinical scanner and 28.6 for the prototype scanner, which is in line with the simulations.

The profile over the spheres of 22 and 17 mm diameter is shown in figure 8(a). The profile was normalized to the total activity in the background of both SPECT reconstructions. The peak of the small sphere in the prototype scanner reached a lower maximum than the clinical scanner. This behavior is confirmed by the T/N ratios for all spheres in figure 8(b), which shows that the relative difference between the scanners increased toward smaller spheres. These results were in agreement with the trends on the T/N ratio observed in the simulation study.

The reconstructions of the anthropomorphic phantom are shown in figure 9. Because the phantom was larger than the FOV of the prototype scanner, it could only be partially reconstructed. Although the bone insert in the prototype scanner did not stand out as much as in the clinical scanner, the lungs were clearly visible. Hence, it was possible to register the CBCT from the prototype scanner to the attenuation map generated by the clinical SPECT/CT. The patient bed was manually removed from the attenuation map for the reconstruction of the prototype scanner.

The SPECT reconstruction of the prototype scanner showed that the extrahepatic deposition was visible. The cold core was distinguishable, but had lower contrast than in the reconstruction of the clinical scanner. Some truncation was present toward the edges of the reconstruction, since the FOV of the gamma camera was smaller than that of the CBCT. Higher noise levels were observed in the liver background volume than in the reconstruction of the clinical scanner.



Discussion

A dual-layer detector that is capable of acquiring simultaneous fluoroscopic and nuclear projections was previously evaluated using planar imaging. This study evaluated via simulations and phantom experiments what image quality can be retrieved when performing SPECT. Although CNR and T/N ratio were lower with the dual-layer scanner, the extrahepatic depositions of the anthropomorphic phantom were distinguished with this system. Furthermore, acquisition of simultaneous SPECT and CBCT was shown to be feasible. This could have advantages in a good integration in the intervention room due to the compact scanner size, intrinsically registered SPECT and CBCT reconstructions, and potential for respiratory motion correction. Acquiring information on the nuclear distribution during the intervention opens up a new area of research: in hepatic radioembolization, for instance, it could lead to single-session procedures.

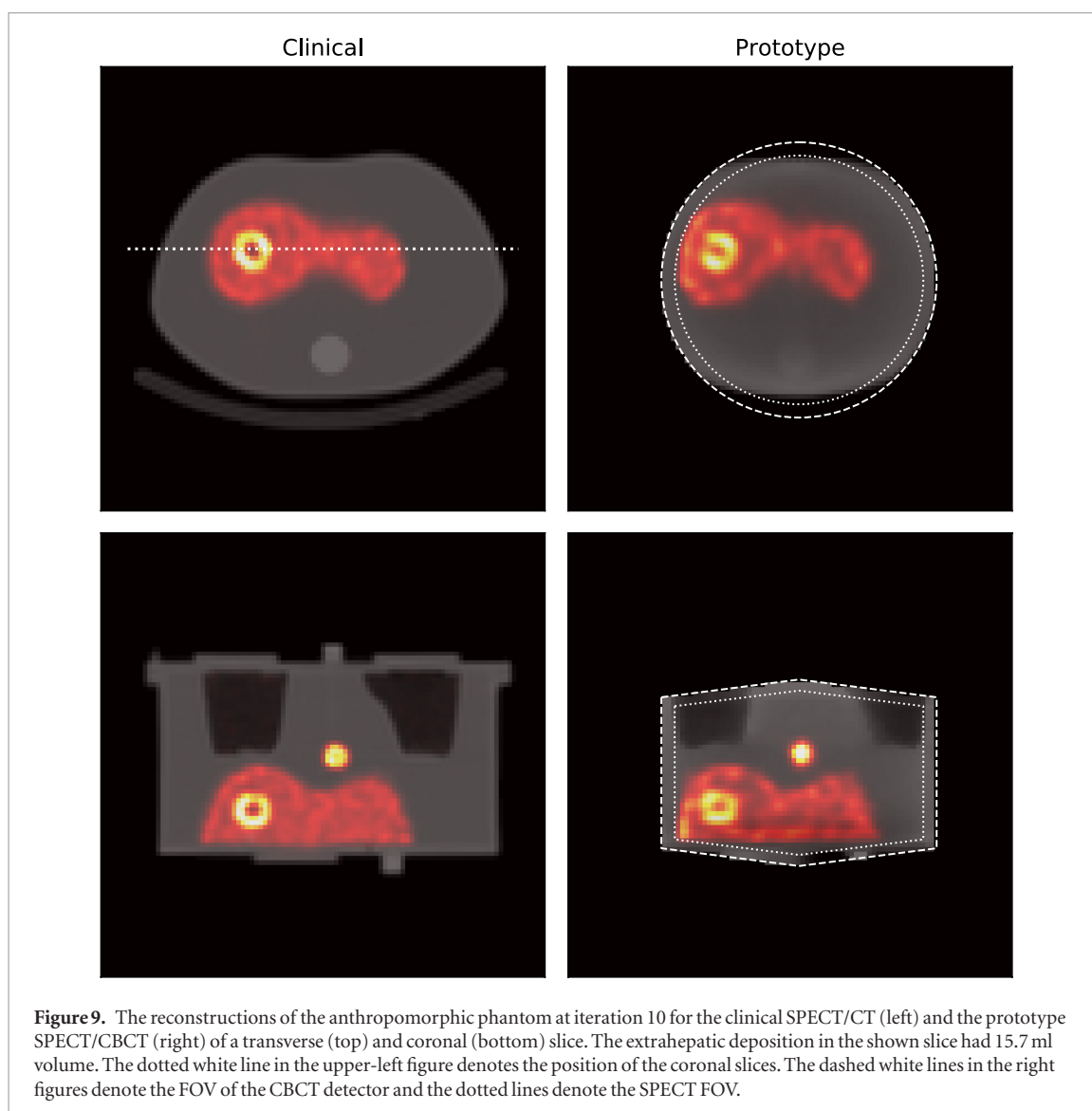
A limitation of this study is that the LSF, often assessed in hepatic radioembolization, could not be measured with the phantom experiments due to the limited FOV of the prototype scanner. This evaluation was, however, performed in the simulation study, which showed that the LSF could be determined within 0.5 percent point, which can be considered clinically sufficient. Since the simulation study showed similar results as the phantom experiments, we are confident that we would be able to accurately determine the LSF in a system with larger FOV.

A further limitation is that only extrahepatic depositions with volumes (4.1, 7.9, and 15.7 ml) and activities (respectively 0.8%, 1.5%, and 2.9% of the total injected activity) close to the median values as encountered in hepatic radioembolization (6.8 ml and 1.3% activity) were evaluated in this study. There is a large spread these values: in the study of Prince *et al* (2015), activities were found from 0.1% to 19.5% of the total injected activity and the volumes ranged from 1.1 to 42 ml. It might be that the dual-layer scanner will not be able to detect the very small, low in activity extrahepatic depositions due to the decrease in visual image quality.

It will depend per procedure whether planar imaging with the dual-layer scanner is sufficient for feedback on the nuclear distribution or that a SPECT scan should be performed. In hepatic radioembolization, we envision that a physician could use planar imaging for determining the lung shunt fraction and to validate whether the correct liver segments are treated, and SPECT for detection of extrahepatic depositions, because of their smaller size. SPECT can, in contrast with planar imaging, also provide quantitative results, which can be beneficial for treatments in which the absolute administered activity is important.

The fluoroscopic image quality of the dual-layer scanner will be lower than that of a conventional scanner, due to the removed anti scattergrid. Accordingly, we will perform the first step of the hepatic radioembolization procedure (i.e. vessel identification and catheter positioning) with a conventional CBCT scanner. The patient bed would be rotated after this step and the administration of activity would then be performed under guidance of the dual-layer scanner, whereupon a SPECT scan will be performed to evaluate the distribution in 3D. In a later phase of the project, we will implement a scatter grid that aligns with the conebeam collimator so that the original CBCT quality might be restored without sacrificing SPECT quality.

The dual-layer scanner might be able to provide respiratory motion compensation, since nuclear and anatomical information is gathered simultaneously. The motion signal over time could be retrieved from the CBCT projections by tracking the lung-liver barrier. The corresponding motion vector field could be then obtained by registering gated CBCT reconstructions to a stationary frame, which could be included in the SPECT reconstruction. This approach was shown to work well in simulations (Dietze *et al* 2018a). The SPECT image quality improvement in phantom experiments will be studied in future work.



To be able to use the proposed scanner in an interventional setting, imaging should be performed quickly, ideally within minutes. The reduction in counts when scanning faster will increase noise in the reconstruction. In the case of hepatic radioembolization, however, quantitative measures as T/N ratio are most important, which are less sensitive to noise. Recent work has shown that one can move towards a substantially reduced imaging time and still obtain quantitative results (van der Velden *et al* 2018). Furthermore, the possibility of acquiring images directly after injection will increase the number of counts as compared with a later imaging session at a clinical SPECT/CT. We expect that imaging within 10 min should be feasible.

Parameterized orbits require measurements of several distances to calculate the orbit from. We aim to perform these measurements automatically in the device under construction, so that potential miscalculations are avoided. A test rotation of approximately 30 s in duration will furthermore be performed before scanning to ensure that no collisions with the patient or bed occur. There is a large freedom in the configuration of orbits. If it appears that more general orbits (e.g. more elliptical) are required, these can be implemented without much effort. At a later stage in the project, the option to perform a body-tracing orbit can be added.

Similar to imaging speed, reconstructions should be performed within minutes to ensure a smooth workflow. In the current implementation, reconstruction takes approximately half an hour for ten iterations with the mentioned image matrix size. With the use of multiprocessing, GPU-based matrix operations, and further code optimization, we expect that Monte Carlo-based reconstruction within 5 min should be achievable.

A different configuration, in which the flat panel is not positioned in front of the gamma camera (and thus is not reducing the gamma transmission and system resolution), could also be used for SPECT, for example using pinhole collimators as in a previous design (Beijst *et al* 2016). However, a primary objective of the proposed scanner is to perform simultaneous planar imaging. This is more straightforwardly achieved with a dual-layer design, since both modalities intrinsically overlap. The dual-layer design furthermore admits of a compact detector that can be mounted on a custom C-arm. The scanner design could potentially be altered between planar imaging

and SPECT during the procedure, but this would introduce extra operations and would limit practical use. This option has therefore not been further studied in this work.

The phantom experiments in this work cannot be directly compared with the results from the simulation study. The physical phantoms were positioned relatively close to the detector in the prototype scanner, in order to enlarge the reconstruction FOV. Such a situation cannot be achieved in a realistic setting, as the patient bed would get in the way. The patient bed would reduce sensitivity due to increased attenuation and reduce resolution due to a larger object-detector distance. The main goal of the experiments was to study the impact of performing simultaneous SPECT/CBCT, which has been shown not to hinder accurate nuclear imaging. We observed in the experiments no systematic artifacts from the removal of the anti scattergrid or the thinning of the back shielding on the fluoroscopic images.

The CBCT reconstruction with the prototype scanner were performed using low dose (50 kVp with 4 mAs for the IQ phantom; 60 kVp with 12 mAs for the anthropomorphic phantom), because we want to limit the extra administered dose to patients. The above settings were found to be the minimum values where attenuation correction or registration could still be correctly performed. The IQ phantom required lower dose than the anthropomorphic phantom, because it is substantially smaller in size.

An increase in CBCT quality could be achieved by increasing the beam strength (both voltage and current). However, at higher beam strengths, the impact of x-ray pulses on the gamma camera will become substantial in the form of afterglow and photomultiplier-tube (PMT) limitations (Koppert *et al* 2018), which will severely reduce the fraction of usable gamma photons. Solutions for this limitation may be found in the modification of PMT circuitry by the introduction of a high-pass filter, mechanical shielding, or the use of different crystals for the gamma camera. For now, the obtained CBCT reconstructions are sufficiently accurate to perform attenuation correction or registration.

This work has focused on the visualization of ^{99m}Tc , because this is the most common isotope in SPECT and also used in the pre-treatment procedure of hepatic radioembolization. Eventually, we want to move towards imaging of the microspheres used in hepatic radioembolization treatment. These isotopes (e.g. ^{90}Y) however radiate at higher energies, which requires thicker collimator septa and increased gamma camera shielding. Both have a major influence on the weight of the detector, complicating the design. For now, we concentrate on ^{99m}Tc to facilitate a fast implementation in the clinic, but work is ongoing to also enable imaging of isotopes with higher energy.

Future work on the proposed dual-layer scanner will be on the development of the custom C-arm, so that the scanner can be used for patient studies. Additionally, it will be investigated whether the optimized flat panel can be manufactured. The gamma camera will be increased in size to enlarge the reconstruction FOV and changes to the PMT circuitry will be made, to cope with higher x-ray fluxes.

Conclusion

Performing simultaneous SPECT/CBCT did not introduce artifacts in either the SPECT or the CBCT reconstructions for the studied situations. SPECT reconstruction quality of the dual-layer scanners was less than that of a clinical SPECT/CT scanner, but extrahepatic depositions with volumes and activities close to the median values encountered in hepatic radioembolization were distinguished from the background activity. The compact design of our system will allow inclusion of the scanner in intervention suite equipment and hence might improve interventional procedures involving radionuclides.

Disclosure

This project has received funding from the European Union's Horizon 2020 research and innovation program under grant agreement no 646734. Philips Healthcare supported this research by providing an adapted flat panel detector. The authors had full control over the data and the information submitted for publication.

ORCID iDs

Martijn M A Dietze  <https://orcid.org/0000-0003-1159-3510>

References

- Bailey D L and Willowson K P 2013 An evidence-based review of quantitative SPECT imaging and potential clinical applications *J. Nucl. Med.* **54** 83–9
- Bailey D L and Willowson K P 2014 Quantitative SPECT/CT: SPECT joins PET as a quantitative imaging modality *Eur. J. Nucl. Med. Mol. Imaging* **41**

- Beijst C, Elschot M, Viergever M A and de Jong H W A M 2016 Toward simultaneous real-time fluoroscopic and nuclear imaging in the intervention room *Radiology* **278** 232–8
- Biguri A, Dosanjh M, Hancock S and Soleimani M 2016 TIGRE: a MATLAB-GPU toolbox for CBCT image reconstruction *Biomed. Phys. Eng. Express* **2** 055010
- Braat A J A T *et al* 2015 ^{90}Y Hepatic radioembolization: an update on current practice and recent developments *J. Nucl. Med.* **56** 1079–87
- de Jong H W A M, Slijpen E T P and Beekman F J 2001 Acceleration of Monte Carlo SPECT simulation using convolution-based forced detection *IEEE Trans. Nucl. Sci.* **48** 58–64
- Dietze M M A, Bastiaannet R, Kunnen B, van der Velden S, Lam M G E H, Viergever M A and de Jong H W A M 2018a Motion compensation in interventional liver SPECT using simultaneous x-ray and nuclear imaging *RSNA 2018* p SSJ22-04 (<http://archive.rsna.org/2018/NuclearMedicine.pdf>)
- Dietze M M A, van der Velden S, Lam M G E H, Viergever M A and de Jong H W A M 2018b Fast quantitative reconstruction with focusing collimators for liver SPECT *EJNMMI Phys.* **5** 28
- Gabr A *et al* 2016 Same-day ^{90}Y radioembolization: implementing a new treatment paradigm *Eur. J. Nucl. Med. Mol. Imaging* **43** 2353–9
- Garin E, Edeline J and Rolland Y 2016 High impact of preferential flow on $^{99\text{m}}\text{Tc}$ -MAA and ^{90}Y -loaded microsphere uptake correlation *J. Nucl. Med.* **57** 1829–30
- Jan S *et al* 2004 GATE: a simulation toolkit for PET and SPECT *Phys. Med. Biol.* **49** 4543–61
- Kennedy A, Coldwell D, Sangro B, Wasan H and Salem R 2012 Radioembolization for the treatment of liver tumors: general principles *Am. J. Clin. Oncol. Cancer Clin. Trials* **35** 91–9
- Klein S, Staring M, Murphy K, Viergever M A and Pluim J P W 2010 Elastix: a toolbox for intensity-based medical image registration *IEEE Trans. Med. Imaging* **29** 196–205
- Koppert W J C, van der Velden S, Steenbergen J H L and de Jong H W A M 2018 Impact of intense x-ray pulses on a NaI(Tl)-based gamma camera *Phys. Med. Biol.* **63** 065006
- Prince J F, van Rooij R, Bol G H, de Jong H W A M, van den Bosch M A A J and Lam M G E H 2015 Safety of a scout dose preceding hepatic radioembolization with ^{166}Ho microspheres *J. Nucl. Med.* **56** 817–23
- Ritt P, Sanders J and Kuwert T 2014 SPECT/CT technology *Clin. Transl. Imaging* **2** 445–57
- Segars W P, Sturgeon G, Mendonca S, Grimes J and Tsui B M W 2010 4D XCAT phantom for multimodality imaging research *Med. Phys.* **37** 4902–15
- Siemens 2010 Symbia S and T System Specifications https://static.healthcare.siemens.com/siemens_hwem-hwem_sxxa_websites-context-root/wcm/idc/groups/public/@us/@imaging/@molecular/documents/download/mda1/ndkw/~edisp/symbia-t-spec-sheet-2010-01977049-02434275.pdf (Accessed: 19 December 2018)
- van der Velden S *et al* 2019 A dual layer detector for simultaneous fluoroscopic and nuclear imaging *Radiology* **290** 833–8
- van der Velden S, Dietze M M A, Viergever M A and de Jong H W A M 2018 Fast technetium-99m liver SPECT for evaluation of the pre-treatment procedure for radioembolisation dosimetry *Med. Phys.* **46** 345–55